· Article · Advances in Polar Science
doi: 10.13679/j.advps.2019.0026 March 2020 Vol. 31 No. 1: 36-42

Laboratory experimental study of water drag force exerted on ridge keel

ZU Yongheng, LU Peng*, YU Miao, CAO Xiaowei & LI Zhijun

State Key Laboratory of Coastal and Offshore Engineering, Dalian University of Technology, Dalian 116024, China

Received 22 July 2019; accepted 27 November 2019; published online 6 March 2020

Abstract With the diminishing Arctic sea ice, the dynamic energy-exchange process between sea ice and ocean gains in importance. Concerning how the ice bottom topography affects the drift of sea ice, it is unclear how the ridge–keel-drag force exerted by seawater changes the momentum balance of sea ice. We thus conducted laboratory experiments to investigate how the local drag coefficient of the ridge keel depends on keel shape and on the relative velocity of ice with respect to seawater. A dimensional analysis is used to obtain the relationship between the local drag coefficient C_r, the Reynolds number Re, the dimensionless keel depth h_0, and the keel slope angle φ. The results indicate that the local drag coefficient C_r is only relevant to Re when $Re < 4000$ and the flow is in the laminar regime. With increasing Re, C_r depends on h_0 and φ, which are independent variables, as the flow transitions to the turbulent regime. The parameterization formulas for C_r are also provided.

Keywords ridge keel, drag coefficient, parameterization, Reynolds number

Citation: Zu Y H, Lu P, Yu M, et al. Laboratory experimental study of water drag force exerted on ridge keel. Adv Polar Sci, 2020, 31(1): 36-42, doi: 10.13679/j.advps.2019.0026

1 Introduction

The Arctic sea ice has become thinner and younger in recent years, particularly in the marginal ice zone (MIZ) (Lindsay and Schweiger, 2015; Granskog et al., 2016; Notz and Stroeve, 2016). The decrease in Arctic ice is a synthetic process combining thermodynamic and dynamic processes (Serreze et al., 2007; Zhao et al., 2018). Thermodynamic processes, which are affected by solar radiation, atmospheric and oceanic boundary layers, and sea-ice characteristics, involve ice growth and melt in extent and thickness (Lu et al., 2016). Dynamic processes also strongly affect the extent of summer sea ice (Lu et al., 2011), resulting in the export of Arctic sea ice through the Fram Strait and Nares Strait by the transpolar drift stream and Beaufort Gyre (Mysak et al., 2001; Krumpen et al., 2019). The thinning of Arctic sea ice has led to a faster drift speed of sea ice, especially in the historically narrow MIZ (Spreen et al., 2011). The drift of sea ice in the MIZ is complex because of the convergence and divergence of sea ice resulting from the regional winds and ocean currents. Atmospheric and oceanic drag coefficients, which are the main contributors to the external force on the sea ice, are two key parameters in the momentum balance of sea ice (Petty et al., 2017).

Research on sea-ice dynamics originated in the polar expeditions of the 19th century. More recent research includes the Arctic Ice Dynamics Joint Experiment in the 1970s and the Marginal Ice Zone Experiment in the 1980s. In the initial studies, drag coefficients were considered to be constants in the eddy correlation method (Shirasawa and Ingram, 1997), the profile method (Andreas and Claffey, 1995; Mcphee, 2002), and the momentum method (Hunkins, 1975; Martinson and Wamser, 1990). Drag coefficients determined by traditional methods depend partly on the

* Corresponding author, E-mail: lupeng@dlut.edu.cn

environmental variations that occur during field observations and ignore sea-ice characteristics such as shape parameters, concentration, and ridge density. In particular, form drag caused by the edges of floes and ridges forms due to floe collisions and is often underestimated by conventional methods, particularly in heavily ridged regions or regions with low sea-ice concentrations (Tsamados et al., 2014). An alternative way to feed the gap is to parameterize sea-ice drag coefficients. Arya (1975) proposed to partition the sea-ice drag force, following which the drag coefficient has been progressively parameterized. Later, sea-ice morphology began to be included in the drag-coefficient-parameterization scheme (Lu et al., 2011; Lüpkes et al., 2012). In addition, these schemes are used in the sea-ice model CICE (Flocco et al., 2017).

The drag force on ridge keels is an essential part of the total drag force exerted on sea ice. Lu et al. (2011) proposed a parameterization scheme for the ridge–keel-drag coefficient that considers the effect of ridge density. In this scheme, the ridge–keel-drag coefficient $C_{\mathrm{W}}^{\mathrm{r}}$ is linear in the local drag coefficient C_{r} of the ridge keel, where the dimensionless parameter C_{r} reflects the fluid properties around a ridge keel:

$$C_{\mathrm{r}} = \frac{F}{\rho A V^2}, \tag{1}$$

where F is the form drag force exerted on the ridge keel in the horizontal direction, ρ is the fluid density, A is the keel-area footprint, and V is the keel-drag velocity. However, the specific expression for C_{r} remains uncertain because of the lack of relevant observations and experimental studies, and this situation has remained unchanged even after the adoption of the parameterization in the CICE model (Tsamados et al., 2014; Martin et al., 2016). The motivation of the present study is thus to identify how the local drag coefficient C_{r} of a ridge keel depends on keel depth, keel slope angle, and fluid velocity. Toward this end, physical modeling experiments were conducted in our laboratory to obtain the relationships between these variables, which has led to a parameterization scheme for the form drag force on a ridge keel.

2 Laboratory experiments

The physical experiments were done in a wave tank located at the State Key Laboratory of Coastal and Offshore Engineering at the Dalian University of Technology, China (see Figure 1). The tank is 0.23 m wide, 4.5 m long, 0.45 m deep, and is constructed from glass panels that form the sides and bottom of the tank. The ridge keel is simulated by an inverted-triangle model made of Plexiglas®. Arrays of pipes line the bottom of the tank and are used to inject fresh water into the tank. The water depth was 0.35 m, and the water in the tank was maintained relatively static. Powered by an electronic stepper motor, the ridge-keel model could move along the water surface at a constant speed.

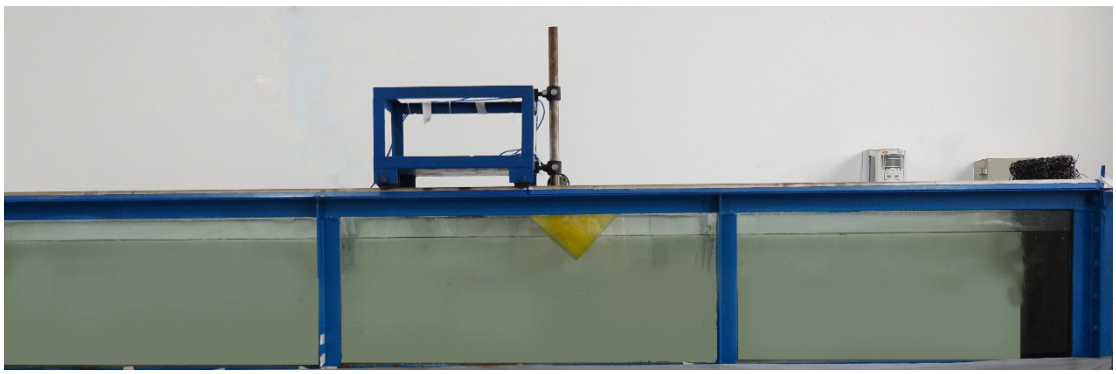

Figure 1 Photograph of laboratory wave tank with ridge-keel model (in yellow).

A tension-compression sensor connected the ridge-keel model with the motor via wire ropes, and a heavy balance serving to increase the model inertia was used to join the end of the model and reduce vibrations of the model. The sensor measurement range was 10 N, and the accuracy was ±0.1% of full scale. Before starting the system, the force tensor was calibrated by using a standard force, following which the drag force exerted on the keel by the fluid was measured with the motor running.

The ice drag consists essentially of two parts: skin drag and form drag (Arya, 1975). Skin drag results from tangential stress in the boundary layer between the ice surface and ocean flow, whereas form drag (exerted on ridge keels) results from the pressure difference between the upstream and the lee of keels. This study simulates the motion of a keel in the tank and is concerned mainly with the form drag on the keel, which is a passive force. If the experiment is to reflect real conditions, the Euler number dynamic similarity law should be applied. However, satisfying the Euler number dynamic similarity is difficult because it is simultaneously affected by the Reynolds number, the Froude number, and boundary conditions.

In the present study, the Reynolds number was selected to account for viscous forces and the keel shape, as done by Schlichting (1960). The drift speed of Arctic sea ice is of the order of 1–100 $\mathrm{cm\cdot s^{-1}}$ (Lepparanta, 2011), and

ridge-keel depths range from 2 to 10 m with a slope angle of 10°–50° (Li et al., 2011). The sea-ice drift speed and keel depth were selected to calculate the Reynolds number, which gives $Re > 20000$ ($Re = Vh/v$, where h is the keel depth and v is the viscosity coefficient). In this experiment, the velocity of the moving model was 1, 3, 6–10, 12, 15, 24, and 30 cm·s^{-1}. The keel penetration into the water was adjusted to 2, 4, 6, 8, and 10 cm. Thus, the Reynolds number for the laboratory experiments covers the range 200–30000. When $Re > 10000$, we consider that the laboratory fluid conditions are similar to those encountered in the real ocean environment. The large range of Reynolds number ensures that the keel-drag laws probe the different fluid regimes, in particular the transition between the laminar and turbulent regimes.

In addition to having similar fluid environments, the boundary conditions of the ice ridge should also be similar to those found in the ocean. Therefore, the boundary conditions, which depend on the shape of the keel, should be consistent with the real conditions. To explore how keel shape affects keel drag for an individual keel, we selected as the key shape parameters the keel depth and slope angle.

The slope angle of the ridge-keel model was set at 20°, 30°, 45°, or 60°. The experiments included 220 trials to cover all flow conditions from laminar to turbulent flow.

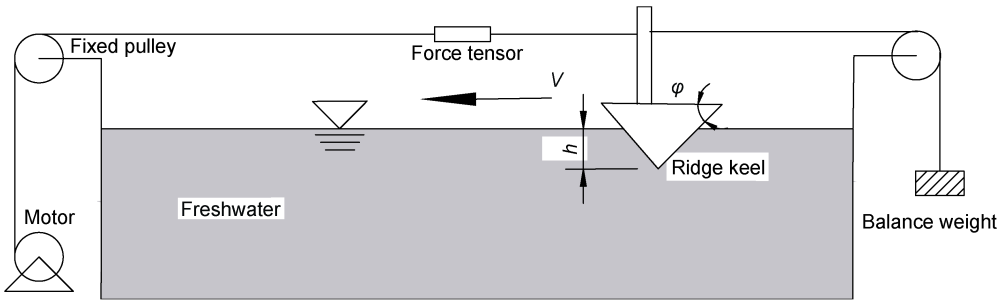

Figure 2 Experimental setup: V is the drift speed of the ridge-keel model, h is the keel depth, and φ is the keel slope angle.

3 Drag force

While moving the ice-ridge model, the drag force on the model was measured by the force sensor at a sampling frequency of 50 Hz. Accelerating the model from rest to a specified speed produces an additional mass force, which is the disturbance term of the drag-force measurements. The starting and ending portions of the raw time-series data are excluded from the analysis because the keel speed varies during the acceleration and deceleration stages. Additionally, vibrations of the model platform could also introduce errors into the drag-force measurements. Thus, the raw time-series data were low-pass filtered to eliminate high-frequency noise, and the mean of the filtered data was taken as the experimental drag force. Figure 3 shows the measured drag force for all experiments.

In general, the drag force increases with increasing speed, keel depth, and slope angle. Simultaneously, Figure 3 shows that, for large keel depth, the drag force exerted on the ice ridge increases significantly with increasing velocity, which is because the drag force exerted on the ice ridge is mainly the form drag force, which is generated by the pressure difference between the front and rear of the ridge keel.

The next section discusses quantitatively how the slope angle, keel depth, and velocity affect the drag force.

4 Discussion

Because cross sections of models have the same shape along the width direction of the wave tank, the problem considered herein is a two-dimensional model with both horizontal and vertical directions. Given an object moving at a constant velocity through a fluid, the drag force exerted on the object depends on the flow conditions (i.e., laminar or turbulent). In this study, the experiments covered both conditions. The experiments in this study investigate a classic problem of fluid mechanics. The momentum flux from ice keel to fluid is described by the Reynolds Averaged Navier–Stokes equations. The drag force F exerted by the fluid on the keel contains two parts: frictional stresses and normal stresses. Viscous stresses along the keel boundary are defined as $\mu(\partial u_i/\partial x_j+\partial u_j/\partial x_i)$, which are in the form of frictional stress. Reynolds stresses are represented by τ_{ij}, according to the Boussinesq hypothesis, and are defined by $\mu_t(\partial u_i/\partial x_j+\partial u_j/\partial x_i)$. Along the keel boundary, the presence of a viscous sublayer results in zero Reynolds stresses, which affects the pressure distribution along the keel boundary. Normal stresses originate from pressure p and $2\mu(\partial u_i/\partial x_i)$ exerted on the keel. Thus, the total drag exerted on the keel is the integral of the frictional and normal stresses along the keel boundary. The boundary conditions of this problem are thus related to keel-shape functions $\eta(x|\ h_w, h, \varphi)$ and keel velocity V, and then total drag force F can be calculated from the velocity and pressure field, which is obtained by solving the Reynolds Averaged Navier–Stokes equations with the given boundary conditions. Thus, $F = f(V, h, h_w, \rho, \varphi, \mu)$.

According to Buckingham's π theorem, this problem has seven variables containing three primary dimensions: mass, length, and time. The measured drag force F depends

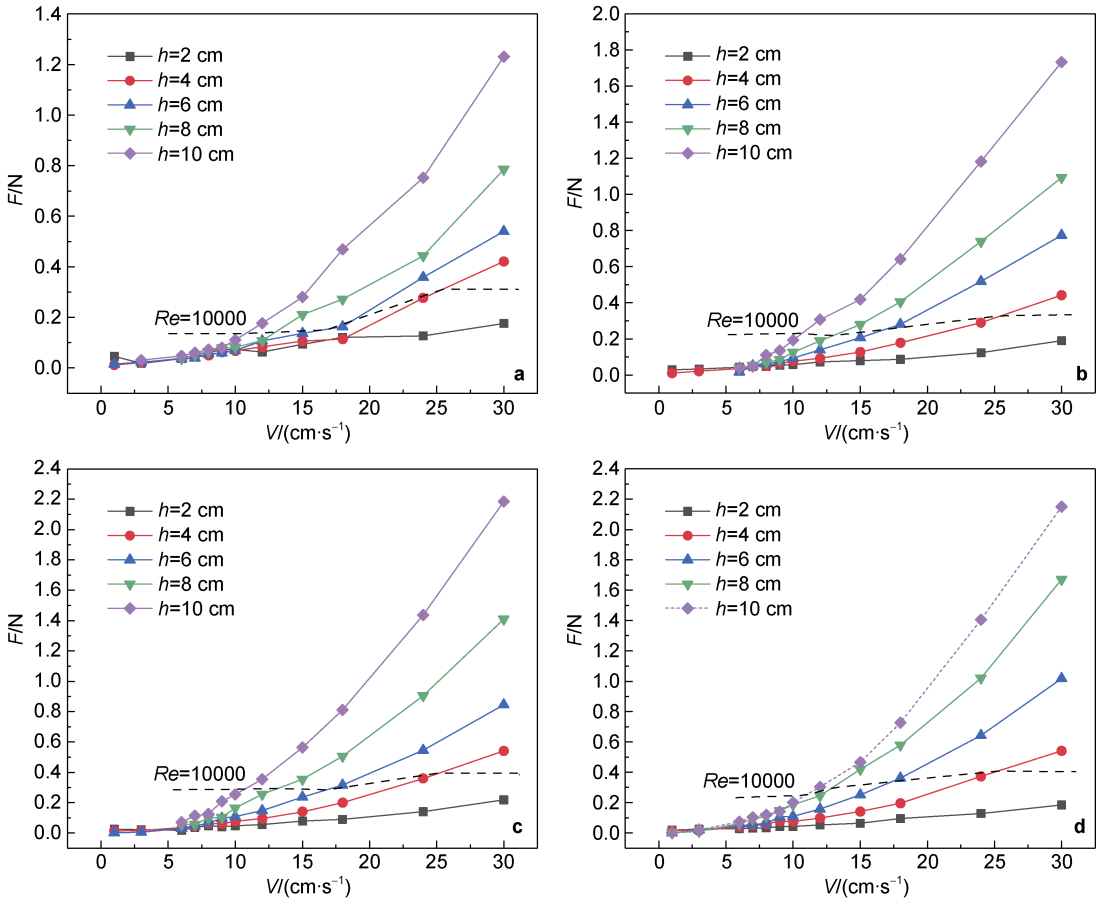

Figure 3 Drag force F as a function of keel velocity V for different keel depths h and slope angles φ = 20° (**a**), φ = 30° (**b**), φ = 45° (**c**), and φ = 60° (**d**). Each panel is divided into two parts by a dashed line representing Re = 10000. The results above this line can be used as a reference for real sea-ice conditions, whereas the results below this line apply only to experimental phenomena.

on the keel velocity V, keel depth h, water depth h_w, and keel slope angle φ. Five variables can be controlled to determine the drag laws between these variables. In addition to these five variables, two parameters, fluid density ρ and viscosity coefficient, reflect the physical properties of the fluid. We thus search for four independent dimensionless parameters to analyze these relationships. This leads to the following dimensional equation:

$$[F]=[\rho]^{x1}[\upsilon]^{x2}[h]^{x3}[V]^{x4}[h_w]^{x5}[\varphi], \quad (2)$$

$$[F]=T^{-2}M,[\rho]=L^{-3}M,[\upsilon]=L^2T^{-1},[h]=L,[V]=L. \quad (3)$$

We then get

$$F=\sum f(\varphi)\rho V^2 h\left(\frac{Vh}{v}\right)^{-x2}\left(\frac{h}{hw}\right)^{-x5}. \quad (4)$$

Equation (4) produces the following four independent dimensionless parameters:

$$C_r=\frac{F}{\rho V^2 h}=f'\left(\frac{Vh}{v},\frac{h}{h_w}\right), R_e=\frac{Vh}{v}, h_0=\frac{h}{h_w}, \text{and } \varphi. \quad (5)$$

The first dimensionless parameter is the local drag coefficient C_r mentioned in Section 1. The second dimensionless parameter is the Reynolds number, which depends on the flow conditions around the keel model. The third dimensionless parameter is the dimensionless keel depth penetrating into the water in the tank, and the last dimensionless parameter is a special parameter that represents the inclination gradient of the ridge keel. Analyses of the drag force consider separately the laminar and turbulent regimes, where the flow conditions are described by the Reynolds number Re, the keel velocity V, the keel depth h, and the fluid viscosity coefficient ν ($\nu \approx 1.002\times10^{-6}$ m^2·s^{-1} in this study), as shown in Equation (5).

The flow resistance exerted on the ridge-keel model consists mainly of pressure resistance (i.e., the form drag force) generated by the pressure exerted by the fluid that flows around the ridge keel and the friction drag force due to the fluid viscosity. These two contributions to the total drag force depend on the Reynolds number Re. When Re is small, the fluid exerts mainly a friction drag force on the keel; in other words, the viscous stress in the fluid dominates the total stress. In this regime, the local drag coefficient depends strongly on the Reynolds number. However, with increasing Re, the flow state transitions to

the turbulent regime and vortex shedding occurs at the back of the object, inducing the von Kármán vortex street so that the form drag force becomes a major part of the total force.

Figure 4 plots $\log_{10}(C_r)$ versus $\log_{10}(0.01Re)$, which reveals a critical Re (≈4000) dividing the plot into two parts. The local drag coefficient C_r, representing the water head loss describes different physical mechanisms from the laminar to the turbulent transition.

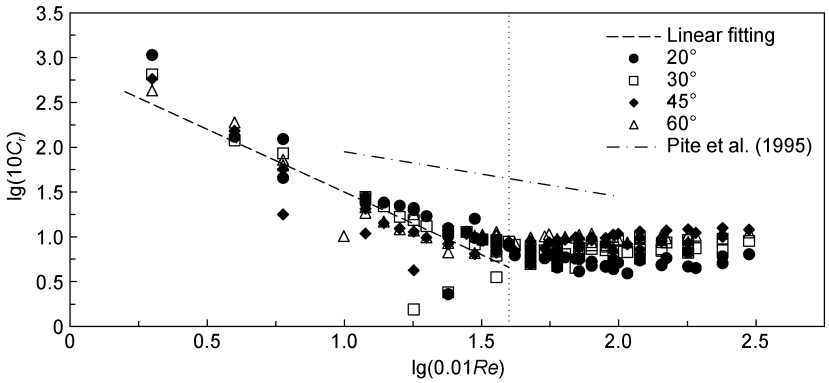

Figure 4 Log-log plot of C_r versus $0.01Re$ for all experimental results. The dotted line shows Pite et al.'s (1995) experimental results and is consistent with the skin friction law. The vertical line at $\log_{10}(0.01Re) = 1.6$ (i.e., $Re = 4000$) marks the transition from laminar flow to turbulent flow.

When $Re < 4000$, the flow is mainly laminar. In the laminar regime, $\log_{10}(10C_r)$ is linear in $\log_{10}(0.01Re)$. Based on the results shown in Figure 4, the keel slope angle φ has little effect on C_r in the laminar regime. C_r decreases rapidly with increasing Re, which is attributed to the friction drag force being dominated by the fluid viscosity. A linear fit in the laminar regime gives

$$\lg(10C_r) = 2.9 - 1.4\lg(0.01Re) \ , \tag{6}$$

which can be simplified to

$$C_r = \frac{a}{Re^b} \ . \tag{7}$$

In this experiment, $a \approx 5000$ and $b = 1.4$. Pite et al. (1995) gives skin friction values of $a = 2.8$ and $b = 0.5$. In this study, we use the larger power for Re than in Pite's formula, so a is three orders of magnitude greater than in Pite's formula. When Re is small, the fluid mainly exerts a drag force on the ridge model; that is, the viscous stress in the fluid dominates the total stress. In addition, the local drag coefficient depends strongly on the Reynolds number.

Conversely, as Re increases above 4000, the flow gradually becomes turbulent. The Reynolds number has less effect on the local drag coefficient C_r, which is now concentrated within a small range.

In the turbulent-flow regime, the streamlines around the model are no longer parallel, and a vortex forms to the lee of the model. The pressure in the vortex zone is lower than the pressure near the front streamline, exerting a form drag force that is much greater than the friction drag force. The total drag force is thus strongly affected by the shape of the model because the shape determines the distribution of the pressure gradient around the boundary. In this study, the two parameters h and φ determine the flow boundary conditions.

Figure 5a shows C_r as a function of V for various keel depths h and for a slope angle $\varphi = 45°$. Figure 5b shows C_r as a function of V for various slope angles φ and for a keel depth $h = 6$ cm. Figures 5a and 5b show that C_r is independent of V for $V > 10$ cm·s^{-1} in the turbulent regime, whereas the two variables h and φ strongly affect C_r.

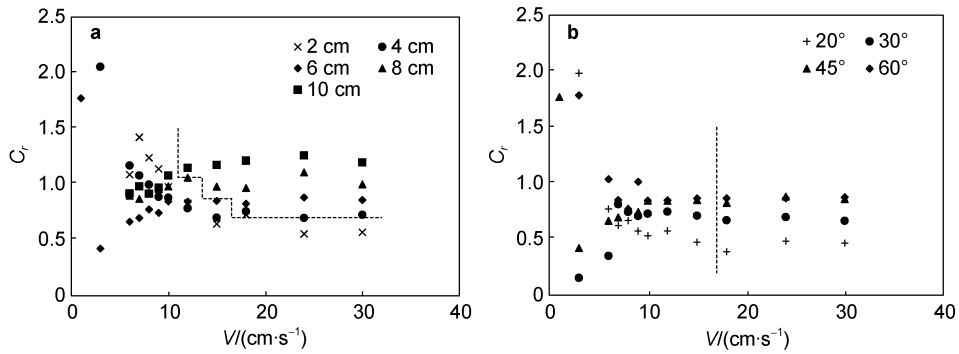

Figure 5 C_r as a function of keel velocity V for various keel depths h and with a keel slope angle $\varphi = 45°$ (**a**) and for various keel slope angles and with a keel depth $h = 6$ cm (**b**). The dashed lines in both panels mark the boundary of $Re = 10000$ between the real ocean and experimental conditions.

Figure 5 shows that C_r depends strongly on h and φ when the flow is turbulent. When h_0 and φ are in the turbulent-flow regime, C_r depends only slightly on Re (see Figure 4), so we may neglect the effect of Re on C_r in the turbulent-flow regime. This gives

$$C_r = f(h_0, \varphi). \quad (8)$$

Figure 6 shows C_r calculated from the mean drag force as a function of h_0 and φ, together with a surface fit. When φ = 20°, the flow in the partial experimental cases transitions from laminar to turbulent, which gives rise to the fluctuations for φ = 20° in Figure 6.

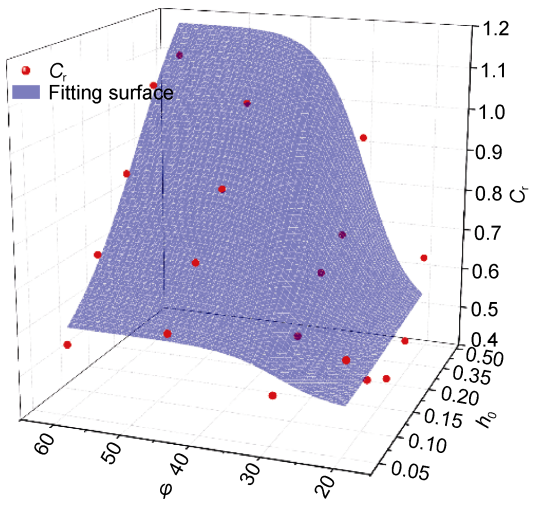

Figure 6 Plot of C_r (Re > 4000) as a function of h_0 and φ and the fitting surface.

The drag coefficient clearly increases with increasing keel depth h_0 and keel slope angle φ. We applied a logarithmic surface fit to obtain an analytical expression for C_r as a function of h_0 and φ. When φ is small (e.g., φ = 20°), C_r is stable around 0.5. Upon increasing φ, the gradient of C_r with respect to h_0 increases and C_r reaches almost 1.1 when h_0 = 0.29, φ = 60°. When h_0 is constant, C_r may be expressed in terms of φ as

$$C_r = c\ln(\varphi) + d, \quad (9)$$

where c and d are parameters related to the keel depth h_0. When h_0 = 0.17 (moderate keel depth in this study), c = 0.4 and d = 0.71, and the mean value of C_r is about 0.67. Gabrecht et al. (1999) analyzed field data and obtained the local drag coefficient for a single ridge sail of C_r = 0.68, which led them also to conclude that a logarithmic function describes how the local atmospheric drag coefficient of a single ridge sail depends on ridge height. Thus, the logarithmic dependence of C_r on h_0 and φ is feasible in the turbulent region, where the shape of the ridge keel strongly affects the local drag coefficient.

5 Conclusion

This paper discusses how the parameters of the ice ridge affect the local drag coefficient, where the parameters include the fluid velocity with respect to the keel, the depth of the ice ridge keel, and the keel slope angle. The experimental results for the drag force exerted on the ice ridge are analyzed dimensionally. The local ridge–keel-drag coefficient C_r depends on the Reynolds number Re, the dimensionless keel depth h_0, and the keel slope angle φ.

When Re < 4000, the flow is laminar. The friction drag force is the main contributor to the total force, and the shape of the keel has little effect on the local drag coefficient. Equation (6) expresses the parameterization that is relevant in the laminar regime.

When Re > 4000, the flow gradually transitions to turbulence. The form drag force now exceeds the friction drag force, and the local drag coefficient becomes sensitive to the shape of the keel, as described by h_0 and φ. In this regime, a logarithm surface fitting is used to express how C_r depends on h_0 and φ.

This paper provides a preliminary discussion of the local drag coefficient of a ridge keel in laboratory experiments. In practice, the smallest Reynolds number for a fluid under a ridge keel is about 10000. In comparison with the experiment results, this interval (Re > 10000) should undoubtedly be in the turbulent regime. Therefore, the local drag coefficient of a ridge keel is a function of keel depth and keel slope angle.

In the future, ridge-keel morphology needs to be considered to express the local drag coefficient, which lays the foundation for the parameterization of the ice-water drag coefficient. The local drag coefficient of a single ice ridge plays an essential role in determining the ice-water drag coefficient. Combined with the lower concentration of sea ice in the Arctic summer MIZ, accurate knowledge of the drag coefficient given the local conditions of sea ice, wind, and current is urgently required for sea-ice forecasting in the climatology model.

Note that this study does not consider how the drag of the ice ridge is affected in reality by the depth of the mixed ocean layer. Thus, further experimental research and theoretical analysis are needed to fully parameterize the ice-water drag coefficient.

Acknowledgments This research was supported by the National Key R&D Program of China (Grant no. 2017YFE0111400), National Natural Science Foundation of China (Grant nos. 41922045 and 41876213), and the Fundamental Research Funds for the Central Universities.

References

Andreas E L, Claffey K J. 1995. Air-ice drag coefficients in the western Weddell Sea: 1. Values deduced from profile measurements. J Geophys Res-Oceans, 100(C3): 4821-4831, doi: 10.1029/94jc02015.

Arya S P S. 1975. A drag partition theory for determining the large-scale roughness parameter and wind stress on the Arctic pack ice. J Geophys Res, 80(24): 3447-3454, doi: 10.1029/jc080i024p03447.

Flocco D, Feltham D L, Schroeder D, et al. 2017. Improved ice-ocean form

drag parameterization in the CICE Model//AGU Fall Meeting, abstract #C21B-1117.

Granskog M, Assmy P, Gerland S, et al. 2016. Arctic research on thin ice: Consequences of Arctic sea ice loss. Eos Trans. AGU, 97(5): 22-26, doi: 10.1029/2016eo044097.

Hunkins K. 1975. The oceanic boundary layer and stress beneath a drifting ice floe. J Geophys Res, 80(24): 3425-3433, doi: 10.1029/jc080i 024p03425.

Krumpen T, Belter H J, Boetius A, et al. 2019. Arctic warming interrupts the Transpolar Drift and affects long-range transport of sea ice and ice-rafted matter. Sci Rep, 9(1): 5459, doi: 10.1038/s41598-019-41456-y.

Lindsay R, Schweiger A. 2015. Arctic sea ice thickness loss determined using subsurface, aircraft, and satellite observations. Cryosphere, 9(1): 269-283, doi: 10.5194/tc-9-269-2015.

Lu P, Leppäranta M, Cheng B, et al. 2016. Influence of melt-pond depth and ice thickness on Arctic sea-ice albedo and light transmittance. Cold Reg Sci Technol, 124: 1-10, doi: 10.1016/j.coldregions.2015. 12.010.

Lu P, Li Z, Cheng B, et al. 2011. A parameterization of the ice-ocean drag coefficient. J Geophys Res-Oceans, 116(C07019): 1-14, doi: 10.1029/2010JC006878.

Lüpkes C, Gryanik V M, Hartmann J, et al. 2012. A parametrization, based on sea ice morphology, of the neutral atmospheric drag coefficients for weather prediction and climate models. J Geophys Res-Atmos, 117(D13112): 1-18, doi: 10.1029/2012JD017630.

Martin T, Tsamados M, Schroeder D, et al. 2016. The impact of variable sea ice roughness on changes in Arctic Ocean surface stress: A model study. J Geophys Res-Oceans, 121(3): 1931-1952, doi: 10.1002/ 2015jc011186.

Martinson D G, Wamser C. 1990. Ice drift and momentum exchange in winter Antarctic pack ice. J Geophys Res-Oceans, 95(C2): 1741-1755, doi: 10.1029/jc095ic02p01741.

McPhee M G. 2002. Turbulent stress at the ice/ocean interface and bottom surface hydraulic roughness during the SHEBA drift. J Geophys Res-Oceans, 107(C10): 8037, doi: 10.1029/2000jc000633.

Mysak L A. 2001. Patterns of Arctic circulation. Science, 293(5533): 1269-1270, doi: 10.1126/science.1064217.

Notz D, Stroeve J. 2016. Observed Arctic sea-ice loss directly follows anthropogenic CO_2 emission. Science, 354(6313): 747-750, doi: 10.1126/science.aag2345.

Petty A A, Tsamados M C, Kurtz N T. 2017. Atmospheric form drag coefficients over Arctic sea ice using remotely sensed ice topography data, spring 2009-2015. J Geophys Res-Earth Surf, 122(8): 1472-1490, doi: 10.1002/2017jf004209.

Pite H D, Topham D R, van Hardenberg B J. 1995. Laboratory measurements of the drag force on a family of two-dimensional ice keel models in a two-layer flow. J Phys Oceanogr, 25(12): 3008-3031, doi: 10.1175/1520-0485(1995)025<3008:lmotdf>2.0.co;2.

Schlichting H. 1960. Boundary layer theory. New York: McGraw-Hill.

Serreze M C, Holland M M, Stroeve J. 2007. Perspectives on the Arctic's shrinking sea-ice cover. Science, 315(5818): 1533-1536, doi: 10.1126/science.1139426.

Shirasawa K, Grant Ingram R. 1997. Currents and turbulent fluxes under the first-year sea ice in Resolute Passage, Northwest Territories, Canada. J Mar Syst, 11(1-2): 21-32, doi: 10.1016/S0924-7963 (96)00024-3.

Spreen G, Kwok R, Menemenlis D. 2011. Trends in Arctic sea ice drift and role of wind forcing: 1992–2009. Geophys Res Lett, 38(L19501): 1-6, doi: 10.1029/2011GL048970.

Zhao J P, Barber D, Zhang S G, et al. 2018. Record low sea-ice concentration in the central Arctic during summer 2010. Adv Atmos Sci, 35(1): 106-115, doi: 10.1007/s00376-017-7066-6.